On the Microscopic Structure of Hole Traps in pMOSFETs

T. Grasser[◇], W. Goes[◇], Y. Wimmer[◇], F. Schanovsky[◇], G. Rzepa[◇], M. Waltl[◇], K. Rott[•], H. Reisinger[•], V.V. Afanas'ev[‡], A. Stesmans[‡], A.-M. El-Sayed[†], and A.L. Shluger[†]

[◇]*TU Wien, Vienna, Austria* [•]*Infineon Munich, Germany* [‡]*KU Leuven, Belgium* [†]*UCL, London, UK*

Abstract

Hole trapping in the gate insulator of pMOS transistors has been linked to a wide range of detrimental phenomena, including random telegraph noise (RTN), $1/f$ noise, negative bias temperature instability (NBTI), stress-induced leakage currents (SILC) and hot carrier degradation. Since the dynamics of hole trapping appear similar in various oxides such as pure SiO_2, SiON, and high-k, the responsible defects should have a related microscopic structure. While a number of defects have been suspected to be responsible for these phenomena, such as oxygen vacancies/E' centers, K centers, hydrogen bridges or hydrogen-related defects in general, the chemical nature of the dominant charge trap remains controversial. Based on extended time-dependent defect spectroscopy (TDDS) data, we investigate the statistical properties of a number of defect candidates using density functional theory (DFT) calculations. Our results suggest *hydrogen bridges* and *hydroxyl E' centers* to be very likely candidates.

Introduction

Frequently studied defects in silica are the oxygen-vacancy-related defects observed in irradiation studies, which have been investigated theoretically [1–4] as well as experimentally [5, 6]. In addition, hydrogen-related defects have been also widely studied [2, 4, 7] and linked to SILC data [2]. On the other hand, the defects contributing to RTN and NBTI have not yet been unanimously identified [8, 9].

Recent TDDS experiments on the defects responsible for RTN and NBTI [10, 11] have revealed crucial features to aid defect identification: Most importantly, defects can show metastability in both the neutral and the positive charge state. Pertinently, some defects were found to behave like switching oxide traps [12], while others have bias-independent emission time constants. Secondly, some defects were found to be volatile, meaning that they can become electrically inactive for random amounts of time, a feature previously observed for RTN [13, 14]. Another intriguing observation is the widely distributed defect properties, consistent with the structural disorder of the amorphous oxides employed in Si technologies. Thus, for a comparison of theory with experiment, it is mandatory to evaluate the statistical distributions of the defect parameters in amorphous materials.

So far, however, only few DFT calculations have been done on amorphous SiO_2 [3, 15–17]. In the following we will investigate the distributed defect parameters obtained from TDDS and compare them with DFT calculations for three defect candidates.

Experimental

As the defect properties vary over a wide range, we have identified and analyzed 35 defects using TDDS in six pMOSFETs ($W \times L = 150\,\text{nm} \times 100\,\text{nm}$, 2.2 nm SiON [10]). Capture (τ_c) and emission (τ_e) times of one extracted defect, A1, are shown in Fig. 1, where our recently suggested [10, 18] four-state non-radiative multiphonon (NMP) model is used to fit the data. The model requires the specification of a configuration coordinate (CC) diagram such as the one shown in Fig. 2 to describe the dynamics of the transitions between, in general, four states. Various simpler cases occur as well, e.g. state 2 could lie higher in energy than state 2', resulting in a 2-state model, or $\varepsilon_{T1'}$ could be too high for state 1' to be reachable, giving a 3-state model.

Depending on the number of accessible states, 5, 7, or 11 fitting parameters are required, see Figs. 3 and 4. However, except for the position of the trap in the oxide, x, and the prefactor k_0 [18], all parameters could in principle be obtained from DFT calculations, *provided the microstructure of the defect was known*. Conversely, DFT parameters can be compared to experiment to help identify possible defect candidates. Due to the large differences in the CC diagrams obtained in amorphous structures, any match has to be validated at the statistical level, which will be attempted here for the first time in this context.

The extracted defect positions and energy levels are shown in a band diagram in Fig. 5. Note that the switching traps have a second energy level, $E_{1'} = \varepsilon_{T1'} - E_T$, which determines if the defect discharges via the pathway $2 \to 1' \to 1$ rather than via $2 \to 2' \to 1$ [19]. Next, the correlation between the capture and emission times, τ_c and τ_e, vs. position is shown in Fig. 6 and Fig. 7. While this weak correlation is dominated by the WKB coefficient, it is important to realize that there is no 1:1 correlation between τ_c and τ_e as assumed in simple SRH-like models [19, 20]. Also, as suggested previously [21], τ_c and τ_e are correlated ($\rho \approx 0.7$), see Fig. 8. Using our NMP model, we observe that defects measured at say 125–175 °C can have very large τ_c and τ_e (≥ 300 years) when extrapolated to room temperature. Similarly, the effective activation energies range from 0.4 to 1.4 eV, see Fig. 9, demonstrating that the large capture/emission times are due to a thermally activated process.

Ab-initio Calculations

While our samples have an SiON dielectric, we performed our calculations for the simplest case, SiO_2, in order to minimize the enormous number of possible defect configurations. However, hydrogen as the most abundant element in Si processing was added, to include frequently suggested H-related defects [2, 7, 9, 14, 22, 23]. This choice is based on the rationale that pMOS/NBTI is very similar in SiO_2, SiON, and HK gate stacks, suggesting common defects to be responsible. Previous calculations [2, 24] have already shown, however, that the natural candidate, the E' center, has a very deep trap-level ($E_V(\text{Si}) - E_T \approx -3.5\,\text{eV}$), making it incompatible with NBTI/RTN.

For our DFT calculations we created large a-SiO_2 structures containing 216 atoms using ReaxFF [25]. To obtain more realistic bandgaps essential for aligning the oxide defect energy levels with the valence band in Si, a non-local PBE0_TC_LRC hybrid functional as implemented in the CP2K code [26] was used, yielding $E_g(SiO_2) = 8.1\,\text{eV}$ (cf. experiment: 8.9 eV).

As a first candidate, we consider the hydrogen bridge, see Fig. 10, which has previously been linked to SILC [2] and NBTI [24] based on calculations in c-SiO_2. In our amorphous structures

all O atoms were each replaced with a single H atom to create 144 defect configurations. Each such defect was checked for having the required 4 states employing a similar criterion as suggested in [15]. For 12 of those defects, the full CC diagram was calculated using the nudged elastic band method [27], requiring on average 2×10^5 CPU hours for each defect.

Next, we checked the reactions of neutral hydrogen with defect-free *a*-SiO_2. Our calculations suggest that for Si-O bonds longer than 1.65 Å, energy can be released by reactions and reconfigurations induced by hydrogen. This confirms previous speculations [7, 28] that under certain circumstances this configuration can also be stable in the *neutral* charge state. As a result, a 3-fold coordinated Si facing a hydroxyl group is obtained, see Fig. 11, which has the 4 required states and is termed *hydroxyl E' center*. For 13 such defects the full CC diagram was calculated in a similar manner as for the hydrogen bridges.

Discussion

The crucial parameter of any defect is the thermodynamic energy level E_T as shown in Fig. 12. In our experimental data, only defects between -1 and 0 eV below E_V(Si) are accessible. Unfortunately, DFT energy levels contain some uncertainty, making precise statements difficult. In our particular case, one could relate the defect levels to E_V(Si) calculated using the same hybrid functional, which would place 60%/75% of our hydrogen bridges/hydroxyl E' centers above E_V(Si) and thus render them permanently positive under NBTI conditions. To retain a larger fraction of our defect population (58%/50%) and thus improve our statistics, we allow for an energy correction of -0.4 eV, corresponding to $\approx 50\%$ our SiO_2 bandgap error (0.8 eV).

Some selected CC diagrams of the calculated defects are shown in Fig. 13. While the E' center shows the required 4 states, due to its energetic position it would remain neutral under typical NBTI conditions. The hydrogen-bridge, on the other hand, is in good agreement with the experimentally observed behavior. This is also visible in Fig. 14 and Fig. 15, which show the calculated emission times and activation energies. Like the hydrogen-bridge, the hydroxyl E' center has CC diagrams compatible with experimental data, see Fig. 16. As such, it also has active defects within the experimental window, both from a time constant perspective (1 μs – 1 ks) as well as from an activation energy perspective (0.5 eV – 1.3 eV), see Fig. 17 and Fig. 18. Experimental data suggest that the defect distributions are much wider than our TDDS window [21, 29], so it is essential to compare the distributions of the parameters rather than single selected defects. The calculated distributions for both defect candidates are in general well in line with the experimental distributions, see Fig. 19. The most significant deviation is observed for $\varepsilon_{22'}$, which determines the emission time constant, but is notably smaller than the experimental values, on average by 0.5 eV. Whether this is an artifact of our bulk amorphous oxide structure or evidence for a different microscopic nature of the defect remains to be clarified.

Experimental data suggest that defects such as hydrogen bridges and hydroxyl E' centers are introduced during processing. As to hydrogen bridges, it has been shown that oxygen vacancies can trap hydrogen, which is available in abundance, thereby forming a hydrogen bridge. A possible mechanism for the creation of hydroxyl E' centers, on the other hand, would be through the reaction of H_2 with defect-free *a*-SiO_2 during high-temperature process steps [30], which can result in a fully passivated defect with two trapped H. Exposure to atomic H could form an active defect in an exothermic reaction with a small barrier, followed by the release of H_2. The calculated barriers for these reactions are consistent with these considerations, see Fig. 20. Subsequent H/H_2 reactions could then explain the observed volatility.

At a first glance, the involvement of hydrogen-related defects in the charge-trapping component of NBTI appears at odds with the experimental observation that the recoverable NBTI component is independent of the hydrogen concentration of the sample [31, 32]. However, even conservative estimations of the hydrogen concentration seem to suggest that hydrogen is available in abundance even in the driest oxides [33]. In such a case the defect concentration would be limited by the availability of oxygen vacancies and stretched Si-O bonds rather than the (very high) hydrogen concentration. If in these previous studies [31, 32] the hydrogen concentration could only be controlled in a limited manner without resulting in very low hydrogen concentrations, then these experiments would not be able to reveal a hydrogen concentration dependence of the recoverable component of NBTI.

Conclusions

In an extensive study we have compared the distributed parameters of possible hole trap candidates against experimental data. Our results suggest *hydrogen bridges* and *hydroxyl E' centers* to be very likely candidates consistent with various observations and allow understanding of the widely distributed defect properties, which is *essential for accurate reliability extrapolations*.

Acknowledgments

The research leading to these results has received funding from the Austrian Science Fund (FWF) project n°23390-M24, the European Community's FP7 project n°261868 (MORDRED), and the Intel Sponsored Research Project n°2013111914. The computational results presented have been achieved in part using the Vienna Scientific Cluster (VSC) and the UK's national high-performance computing service HECToR and Archer via the Materials Chemistry Consortium (EPSRC EP/F067496). Valuable discussions with P. Lenahan and J. Campbell are gratefully acknowledged.

References

[1] F. Feigl *et al.*, Solid State Comm. **14**, 225 (1974).
[2] P. Blöchl, PRB **62**, 6158 (2000).
[3] C. Nicklaw *et al.*, T-NS **49**, 2667 (2002).
[4] D. Fleetwood *et al.*, T-ED **49**, 2674 (2002).
[5] D. Griscom, PRB **22**, 4192 (1980).
[6] P. Lenahan *et al.*, T-NS **48**, 2101 (2001).
[7] J. de Nijs *et al.*, APL **65**, 2428 (1994).
[8] J. Campbell *et al.*, T-DMR **7**, 540 (2007).
[9] M. Houssa *et al.*, APL **90**, 043505 (2007).
[10] T. Grasser *et al.*, in *IRPS* (2010), pp. 16–25.
[11] T. Grasser *et al.*, in *IRPS* (2014), pp. 4A.5.1–4A.5.7.
[12] J. Conley Jr. *et al.*, T-NS **42**, 1744 (1995).
[13] M. Uren *et al.*, PRB **37**, 8346 (1988).
[14] T. Grasser *et al.*, in *IEDM* (2013).
[15] Z.-Y. Lu *et al.*, Phys. Rev. Lett. **89**, 285505 (2002).
[16] A. Alkauskas *et al.*, Physica B **401-402**, 546 (2007).
[17] A. Kimmel *et al.*, in , R. Sah *et al.* (Ed.) (ECS T, 2009), Vol. 19, pp. 2–17.
[18] W. Goes *et al.*, in *BTI*, T. Grasser (Ed.) (Springer, 2014), pp. 409–446.
[19] T. Grasser, MR **52**, 39 (2012).
[20] A. McWhorter, S.Surf.Phys 207 (1957).
[21] T. Grasser *et al.*, in *IEDM* (2011), pp. 27.4.1–27.4.4.
[22] R. Stahlbush *et al.*, T-NS **41**, 1844 (1994).
[23] V. Afanas'ev *et al.*, JAP **78**, 6481 (1995).
[24] F. Schanovsky *et al.*, in *SISPAD* (2013), pp. 1–4.
[25] A. van Duin *et al.*, J.Phys.Chem.A **105**, 9396 (2001).
[26] M. Guidon *et al.*, J.Chem.Theor.Comp. **5**, 3010 (2009).
[27] G. Henkelman *et al.*, J.Chem.Phys. **113**, 9901 (2000).
[28] V. Afanas'ev *et al.*, PRL **80**, 5176 (1998).
[29] G. Pobegen *et al.*, T-ED **60**, 2148 (2013).
[30] V. Afanas'ev *et al.*, J.Electrochem.Soc. **148**, 279 (2001).
[31] V. Huard, in *IRPS* (2010), pp. 33–42.
[32] T. Aichinger *et al.*, in *IRPS* (2010), pp. 1063–1068.
[33] J. Krauser *et al.*, J.Non-Cryst.Solids **187**, 264 (1995).
[34] K. Huang *et al.*, Proc.R.Soc.A **204**, 406 (1950).

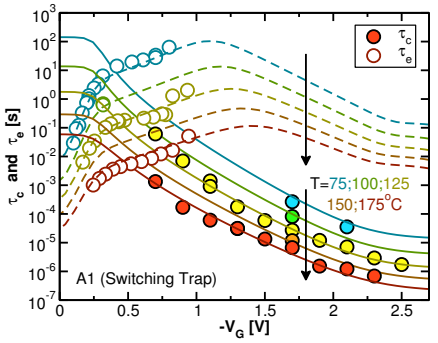

Fig. 1: The capture and emission times (symbols) of trap A1 extracted over a wide temperature and bias range. Our four-state non-radiative multiphonon model [10, 18] can describe the data very well (lines). Note the strong temperature activation as well as the strong bias-dependence of the emission time below $V_{th} \approx 0.5\,V$ and the saturation of the capture time at high biases.

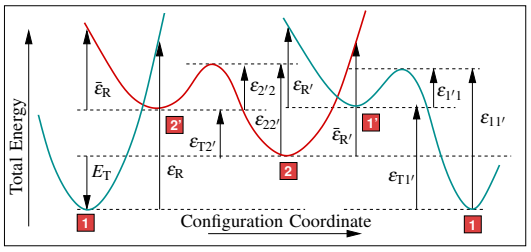

Fig. 2: Following the Born-Oppenheimer approximation we use potential energy surfaces along 1D configuration coordinates (CC) in the various states to describe the transitions using non-radiative multiphonon [19, 34] theory (1 ↔ 2' as 2 ↔ 1') and transition-state theory (2' ↔ 2 and 1' ↔ 1). The CC diagram of a typical four-state defect is specified by eleven fitting parameters but describes the bias-, temperature- and frequency dependence of the capture and emission times. In addition, the position of the trap into the oxide (x), the capture cross section k_0, and an attempt frequency ($\nu = 10^{13}\,s^{-1}$) need to be specified to fully define the transitions [18, 19].

Par	A1	Min	Mean	Max	Unit	
E_T	-0.08	-0.7	-0.36	0.07	eV*	2-State
ε_R	3.22	0.37	1.43	5.34	eV	
$\bar{\varepsilon}_R$	2.95	0.31	2.14	5.05	eV	
$\varepsilon_{T2'}$	0.25	0.16	0.37	0.88	eV	3-State
$\varepsilon_{2'2}$	0.56	0.01	0.63	1	eV	
$(\varepsilon_{22'})$	0.81	0.19	0.99	1.3	eV	
$\varepsilon_{T1'}$	0.31	0.24	0.68	1.82	eV	Full 4-State
$\varepsilon_{R'}$	0.38	0.09	0.82	1.48	eV	
$\bar{\varepsilon}_{R'}$	0.38	0.15	1.09	2.59	eV	
$\varepsilon_{11'}$	1.05	0.94	1.29	1.88	eV	
$(\varepsilon_{1'1})$	0.75	0.06	0.61	0.9	eV	
x	-0.61	-0.04	-0.68	-1.04	nm	
k_0	10^{-9}	10^{-14}	10^{-7}	10^{-6}	eV m^3/s	

Could be calculated by DFT
Remaining fit parameter
*relative to E_V
() overdetermined

Fig. 3: From the 11 parameters required for each defect, 9 can be in principle obtained from DFT, provided the microstructure and it variations are known. Shown are the parameters of defect A1 together with their distribution. Not all states may be accessible, reducing the general 4-state model to a 3- or even 2-state model.

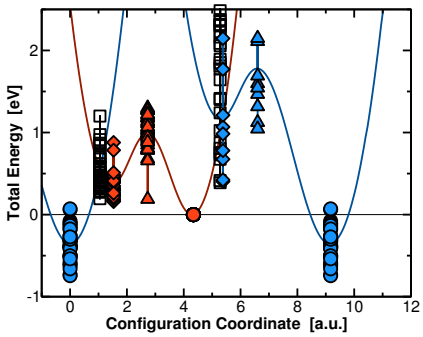

Fig. 4: The average CC diagram as shown in Fig. 2 extracted from 35 defects together with the distribution of the individual barriers with the energy measured relative to E_V(Si). Many distributions are rather wide (about 1 eV).

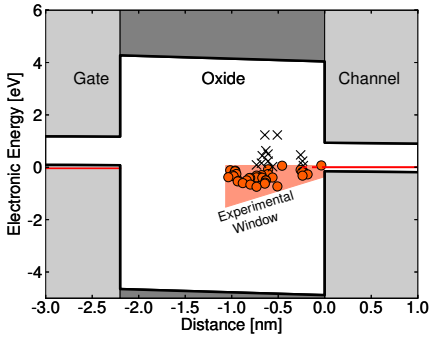

Fig. 5: The trap-levels E_T (circles) and $E_{1'} = \varepsilon_{T1'} - E_T$ (crosses) versus x coordinate of the 35 extracted TDDS defects in a band diagram. The energy is measured relative to E_V(Si). Only traps within the experimental window defined by V_{stress}^{max} are accessible.

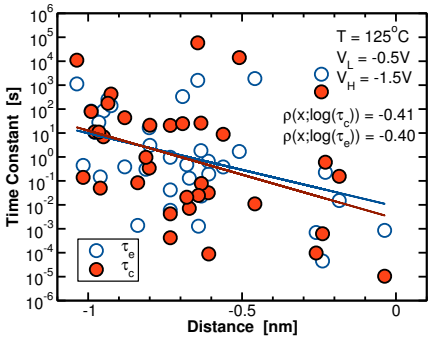

Fig. 6: A weak correlation between the extracted time constants and the position of the trap is observed. While this correlation is dominated by the WKB coefficient, no 1:1 correlation between τ_c and τ_e is obtained.

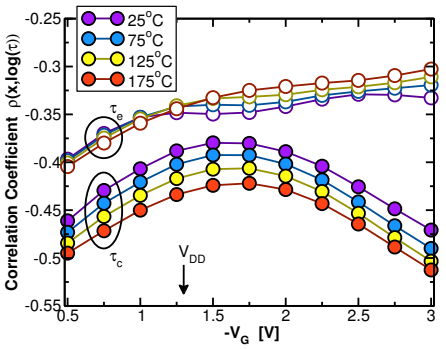

Fig. 7: The correlation coefficients $\rho(x, \log(\tau_e))$ and $\rho(x, \log(\tau_c))$ are small and depend weakly on bias.

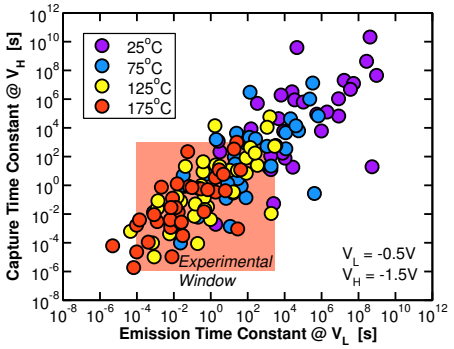

Fig. 8: A clear correlation between the extracted capture and emission times is observed ($\rho \approx 0.7$).

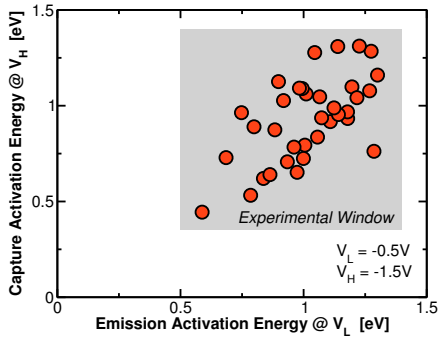

Fig. 9: The effective capture and emission activation energies show a similar correlation and distribution. The experimental window is shown for later reference, cf. Fig. 15 and Fig. 18.

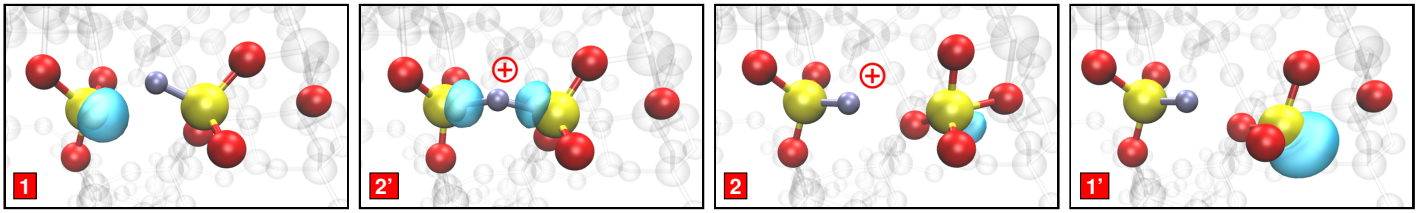

Fig. 10: The four states of the hydrogen bridge: In the initial configuration 1, H (silver) sits between two Si atoms (yellow) which themselves are surrounded by three O atoms (red). The electron density of the localized Kohn-Sham-eigenstate is shown as turquoise 'bubbles'. *Upon hole capture* the defect can go into the metastable state 2', where the Si atoms move closer together. Depending on the gate bias, the defect either goes back to state 1 or, *eventually into the stable positive state 2*, where the right Si has moved through the plane of its three O neighbors, forming a puckered configuration by bonding to the O in the far right. In the metastable state 1', the defect is neutralized but remains in the puckered configuration.

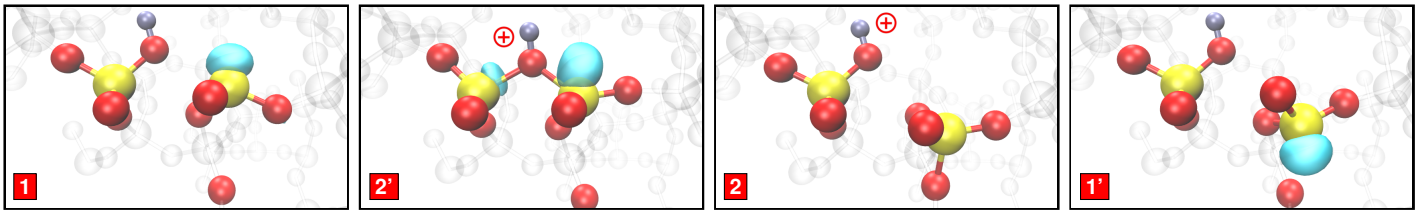

Fig. 11: The four states of the hydroxyl E' center: In the neutral configuration 1, a hydroxyl group sits at the left Si while the other carries a dangling bond. After hole capture, in state 2', the dangling bond has lost its electron and reforms the Si-O-Si bridge, resulting in the typical proton sitting on a bridging O. In state 2, the right Si moves through the plane of its O neighbors, forming a bond with the O in its back. In state 1', the dangling bond is restored but points into the other direction.

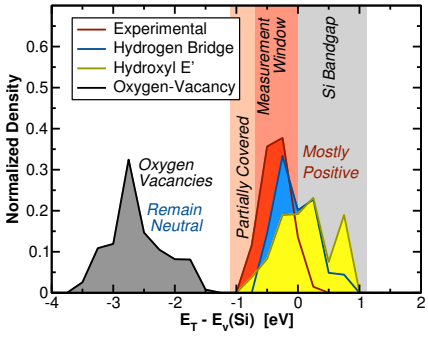

Fig. 12: The fundamental parameter which decides on which trap can be charged for a certain stress (V_G^H) and recovery (V_G^L) combination is the energy level E_T. Clearly, the oxygen vacancy/E' center is too low in energy, while both the hydrogen bridge and the hydroxyl E' center are in good agreement with the data inside the experimental window. Recall the uncertainty in DFT energy-levels and the -0.4eV energy shift used.

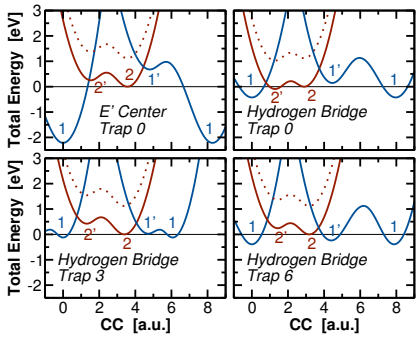

Fig. 13: Some selected DFT CC diagrams for the hydrogen bridge in a-SiO_2, all of which being different, reflecting the amorphous nature of the oxide. The CC diagram of the E' center is also shown at the top-left for comparison, for which state 1 is too low, resulting in a permanently neutral trap.

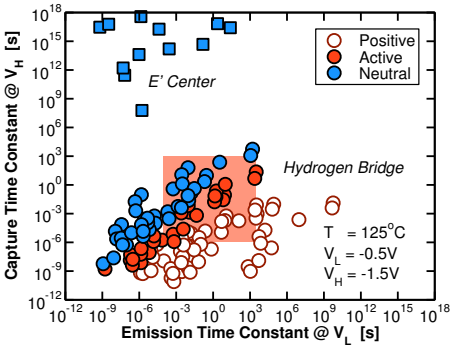

Fig. 14: The theoretical capture and emission times at stress and recovery bias for the defects in Fig. 13. Each DFT defect is considered at 10 random locations in the oxide between 0 and $-t_{ox}/2$. Some defects are energetically too low and remain neutral (blue circles), some are in the active region and can charge and discharge (red circles), while some are too high in energy and are always positive (empty circles). The oxygen vacancy cannot become charged during typical stress conditions and thus remains neutral.

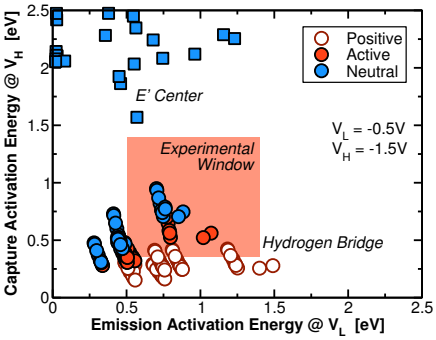

Fig. 15: The theoretical effective capture and emission activation energies for the hydrogen bridge and the regular E' center. While the E' centers would remain neutral under typical NBTI conditions, the hydrogen bridge would be visible in the experimental window.

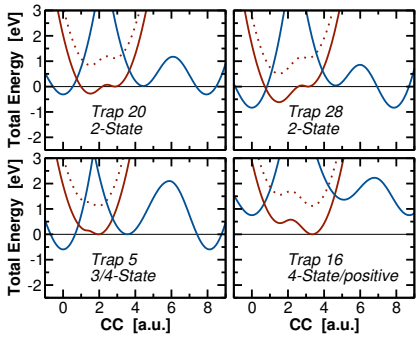

Fig. 16: The DFT CC diagrams of four selected hydroxyl group E' centers. Clearly, marked differences exist. From 13 defects, 3 are found to have all 4 required states in addition to sensible barriers separating them.

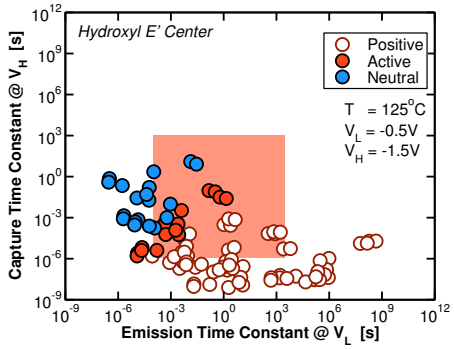

Fig. 17: The theoretical capture and emission time map of the hydroxyl group E' center. Just like the hydrogen bridge, the hydroxyl E' center would be visible in the experimental window.

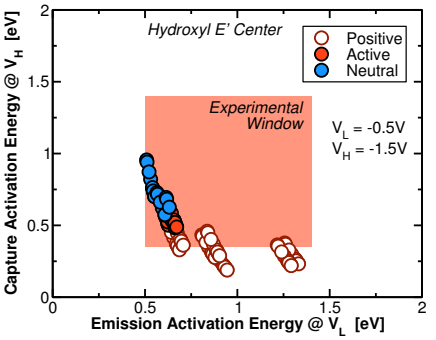

Fig. 18: The theoretical effective capture and emission activation energies for the hydroxyl E' center. Just like the hydrogen bridge, the hydroxyl E' center would be inside the experimental window.

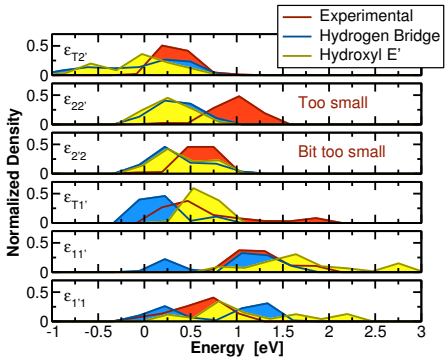

Fig. 19: Comparison of the experimental and theoretical barriers. While overall good agreement is obtained, the theoretical barrier $\varepsilon_{22'}$ is too small in general. Note that the defects with negative $\varepsilon_{T2'}$ are 2-state defects at the border of our experimental window.

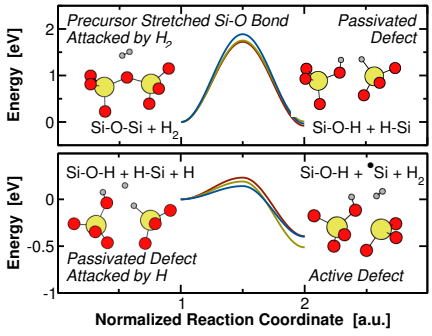

Fig. 20: Possible creation scenario of the hydroxyl E' center during high-temperature processing via the attack of a stretched Si-O-Si bond by H_2, which is later attacked by H to eventually form the active defect. Creation is limited by the precursor-density, not the H concentration [31, 32].